Article

Microstructure and wear resistance of multi-layer Ni-based alloy cladding coating on 316L SS under different laser power

Qian Shaoxiang[1, 2*], Zhang Yongkang[1, 3*], Dai Yibo[4], Guo Yuhang[4]

1 College of Mechanical Engineering, Jiangsu University, Zhenjiang 212013, China; ujsqiansx@163.com (S.-X.Q.); zhangykujs@163.com (Y.-K.Z.);

2 School of Modern Equipment Manufacturing, Zhenjiang College, Zhenjiang 212028, China; qiansx@zjc.edu.cn (S.-X.Q.);

3 School of Electromechanical Engineering, Guangdong University of Technology, Guangzhou 510006, China; ykzhang@gdut.edu.cn (Y.-K.Z.);

4 School of Materials Science and Engineering, Jiangsu University of Science and Technology, Zhenjiang, 212003, China; 199060030@stu.just.edu.cn (Y.-B.D.); guoyuhang@just.edu.cn (Y.-H.G.).

* Correspondence: qiansx@zjc.edu.cn; Tel.: +86-511-8440-1188

Abstract: Three kinds of Ni based alloy cladding coatings were prepared on 316L stainless steel at different power. The microstructure of the cladding layer was observed and analyzed by XRD, metallographic microscope and SEM. The hardness of the cladding layer was measured, and the wear resistance of the cladding layer was tested by friction instrument. The results show that the effect of laser cladding is good and the cladding layer has a good metallurgical bonding with the substrate. Different microstructures such as dendritic and equiaxed grains can be observed in the cladding layer. With the increase of laser power, more equiaxed and columnar dendrites can be observed. The phase composition of the cladding layer is mainly composed of γ - Ni solid solution and some intermetallic compounds such as Ni_3B, Cr_5B_3 and $Ni_{17}Si_3$. The results of EDS show that there are some differences in the distribution of C and Si between dendrites. The hardness of the cladding layer is about 600 $HV_{0.2}$, which is about three times of the substrate (~ 200 $HV_{0.2}$). Through the analysis of the wear morphology, the substrate wear is serious, there are serious shedding, mainly adhesive wear and abrasive wear. However, the wear of cladding layer is slight, which is abrasive wear, and there are some grooves on the surface.

Keywords: Additive manufacturing; Ni based alloy cladding layer; 316L stainless steel; Multilayer laser cladding; Wear properties

1. Introduction

316L stainless steel is a typical low-carbon austenitic stainless steel with good mechanical properties and excellent corrosion resistance, which is widely used in aerospace, chemical, nuclear industry and marine engineering [1-4]. However, due to its weak hardness and wear resistance, its application is greatly limited [2]. Therefore, surface strengthening of 316L stainless steel is one of the most important and essential methods to solve this problem. The commonly used surface strengthening methods of metal materials include strain strengthening [5], surface ultrasonic strengthening [6], surface nanocrystallization [7-9], surface carburizing strengthening [10, 11] and plasma nitriding strengthening [12, 13]. However, these processes are costly and complex, or cause deposition phase and martensitic transformation, thus affecting the corrosion resistance of stainless steel [14, 15].

Preprints (www.preprints.org) | NOT PEER-REVIEWED | Posted: 22 December 2020 doi:10.20944/preprints202012.0549.v1

Different from the above technology of surface modification based on substrate to achieve performance improvement, the technology of material surface modification through cladding layer has entered the field of vision of many researchers. Traditional surface modification cladding technologies include flame spraying [16], ion spraying [17], submerged arc welding (SAW), shielded metal arc welding (SMAW) [18], surface plating [19], etc. However, there are some common problems in these technologies: the bonding force between the base material and the cladding layer material is poor, the porosity defect is easy to appear, and the dilution rate is too high [20]. In addition, if hard chromium plating (HCP) in common surface plating processes can produce toxic and carcinogenic $Cr6^{+}$, its use is also subject to more and more restrictions [21]. The emergence of Laser Cladding Technology (LC) overcomes these shortcomings. Laser cladding (LC) technology is a kind of additive (AM) manufacturing process, also known as direct metal deposition, which uses high-power laser to melt powder / wire and substrate together to obtain cladding layer with good metallurgical bonding performance [2, 22, 23]. Due to the high quality characteristics of low porosity, low dilution ratio and crack free, laser cladding has been widely used to prepare various high-performance composite cladding layers [24].

In the selection of cladding layer materials, Ti based, Co based, Fe based and Ni based alloy powders are widely used. The Ni based alloy can not only provide higher hardness to improve the wear resistance of the material [25], but also improve the yield strength of the material at high temperature, which is matched with the properties required by 316L stainless steel in different environments. In addition, the good corrosion resistance provided by the addition of alloying elements (such as Cr) also has good compatibility with the application environment of 316L stainless steel [26]. Therefore, the cladding of Ni based alloy on 316L stainless steel has attracted some researchers' attention. Chang et al. [27] studied the microstructure and mechanical properties of Ni-Cr-si-B-Fe composite cladding layer prepared by laser cladding. It was found that the cladding layer was mainly composed of amorphous phase and γ-(Fe, Ni) solid solution phase, and the cladding layer showed excellent wear resistance due to the existence of amorphous phase. Moskal et al. [28] laser cladding the NiCrAlY cladding layer on Inconel625 alloy and 316L stainless steel, and the cladding layer with good metallurgical bonding with the substrate was obtained. Only in 316L upper cladding layer, strong epitaxial growth was observed. At the same time, the cladding layers of two different substrates had dendrite and interdendritic zone structure rich in different alloy elements. N. Jeyaprakash et al. [4] studied the laser cladding process of cobalt and nickel based hard micro layers on 316L stainless steel substrate, and found that the wear resistance of nickel based cladding was better than that of cobalt cladding and substrate. Wang et al. [1] studied the corrosion behavior of Ni-Cr-Mo laser cladding layer, 316 stainless steel and X70 Steel in simulated solution of H_2S and CO_2. The Ni-Cr-Mo cladding layer has uniform and dense microstructure, and the morphology does not change after corrosion, showing better corrosion resistance than 316L stainless steel and X70 steel.

Although there are some reports about laser cladding of Ni based alloy on 316L stainless steel, its quantity is relatively small. Therefore, in this study, Ni-Cr-B-Si-C-Fe was selected for multi-layer laser cladding on 316L stainless steel. The phase composition, microstructure evolution and hardness of the cladding layer were investigated by XRD, SEM and microhardness tester. In addition, the wear behavior of laser cladding coating was studied by ball on plate tribometer, and the wear mechanism was discussed and analyzed.

2. Experimental procedure

Commercial Ni based alloy (Ni-Cr-B-Si-C-Fe) powder was used as cladding material. The SEM image of the powder was shown in Figure 1. It can be seen that the shape of the powder is almost equiaxed spherical, and the size is about 50 ~ 150 μm. 316L stainless steel cut into 80 mm×50 mm×10 mm (thickness) was applied as the substrate. Before cladding, the substrates were polished with 1000 mesh SiC sandpaper, and sandblasting technique (Al2O3 ceramic particles) was used over the substrate to have a surface roughness of 10 μm. Then, they were soaked in acetone to remove oil,

Preprints (www.preprints.org) | NOT PEER-REVIEWED | Posted: 22 December 2020 doi:10.20944/preprints202012.0549.v1

washed with alcohol and dried to keep the surface clean. The chemical composition of 316L stainless steel and Ni based alloy powder were shown in Table 1.

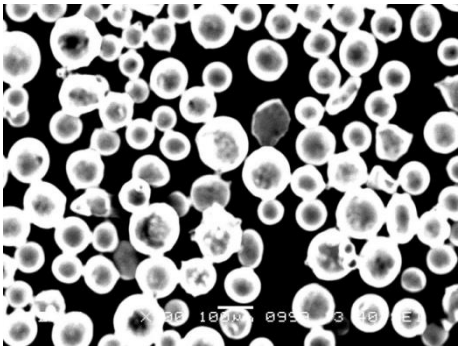

Figure 1. The morphology of Ni-base alloy powders.

Table 1. Chemical composition of 316L stainless steel and powder. (wt%)

Materials	C	P	Cr	S	Mn	Mo	B	Si	Ni	Fe
316L SS	0.023	0.034	16.4	0.57,	1.37	2.16,	--	0.69	10.03	Bal.
Nickel alloy	0.03	--	6.00	--	--	--	3.00	1.50	Bal.	0.38

RFL-C3300 (Raycus, Wuhan) high power continuous fiber laser device was used in laser cladding test. DPSF-2 powder feeder was used to feed powder synchronously in an oblique direction, and argon was used as power source to accurately send powder to laser spot. During cladding process, argon was used to protect molten pool to avoid oxidation. Three different parameters, named LC1, LC2 and LC3, were used for cladding experiment. The detailed parameters were listed in Table 2. The cladding layer was divided into three layers. The first layer and the third layer were along the length direction of the plate, and the second layer was along the width direction of the plate. The sample produced by cladding is shown in Figure 2.

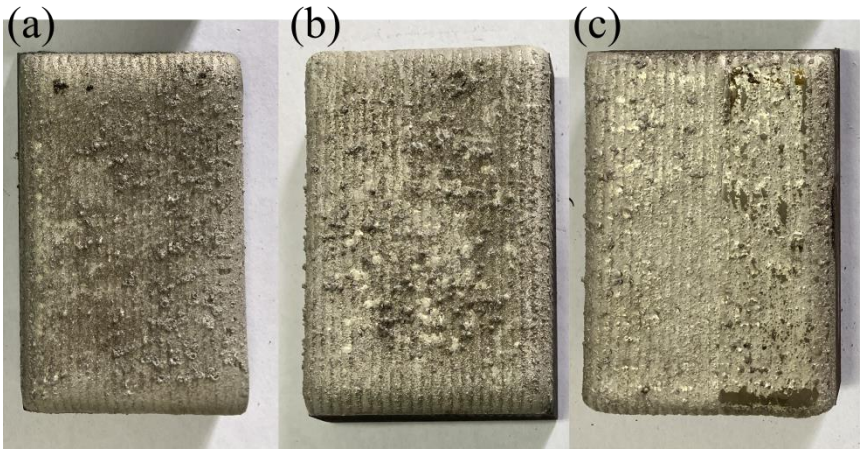

Figure 2. Macroscopic morphology of three cladding coatings (a) sample LC1; (b) sample LC2; (c) sample LC2.

Table 2. Different parameters of laser cladding.

Samples	Laser power (kW)		Powder feed rate (g/min)	Scanning velocity (mm/s)	Spot diameter (mm)	Gas flow rate (L/min)	Overlap rate
	1st layer	2nd & 3rd					

 doi:10.20944/preprints202012.0549.v1

LC1	1.8	2.0	30	5	4	15	50%
LC2	1.8	2.2	30	5	4	15	50%
LC3	1.8	2.4	30	5	4	15	50%

After cladding, the samples were cut, cleaned and degreased with acetone alcohol, and then a standard metallographic sample preparation process (grinding, polishing, washing and drying) was carried out to obtain mirror-surface metallographic samples. The phase identification of cladding layer was performed by X-ray diffractometer (XRD) with a Cu-k α radiation at a voltage of 40 kV. The micromorphology of the cladding layer was observed by JSM-6480 tungsten filament scanning electron microscope (SEM) and ZEISS Merlin compact field-emission scanning electron microscope (FE-SEM), and the element content in the micro area was measured by their equipped energy dispersive spectrometer (EDS). KB-30S-FA Automatic Vickers Hardness Tester was used to test the hardness of the cladding layer and the substrate with the applied pressure of 0.2 kg and the holding time of 15 s. The dry sliding ball-on-plate wear behavior of the cladding layer and the substrate were studied by UMT-2 high-temperature friction and wear tester. For the dry sliding friction test, the sliding time is 1800 s, the relative speed between coating and counter-body is 10 mm/s, and the diameter of the counter-body ball is 10 mm. Finally, the three-dimensional morphology of wear marks was observed by LEXTOLS4000 confocal laser scanning microscope, and the micro wear morphology was observed through SEM.

3 Results and discussion

3.1 Microstructure observation and analysis

The process of the first cladding layer in the three samples is the same. The microstructure of the interface between the substrate and the cladding layer in LC1 is observed, and the SEM image is shown in Figure 3. It can be seen that the cladding layer has good metallurgical bonding with the matrix material, and some small pores are randomly distributed in the cladding layer. Planar and cellular crystals can be observed at the substrate cladding interface, and similar structures have been observed in Li [29] et al. On multilayer laser cladding of 308L stainless steel, which is attributed to the "flat interface growth mode." Two main parameters can be used to explain the microstructure evolution, i.e. temperature gradient G and growth rate R. the change of G/R ratio will change the solidification mode, resulting in the change of microstructure morphology and size [30]. At a large G/R ratio, planar crystals are formed, and with the decrease of G/R ratio, cellular crystals are formed. In addition, there is no heat accumulation during the first layer cladding. At this time, the maximum value of G and the minimum value of R appear at the bottom of the molten pool, and the planar crystals morphology is formed. With the decrease of G/R ratio, cellular crystals appear between the planar crystals and the liquid phase. However, it can be seen that such morphology is small-scale, only within 10-20 μm above the interface.

Preprints (www.preprints.org) | NOT PEER-REVIEWED | Posted: 22 December 2020 doi:10.20944/preprints202012.0549.v1

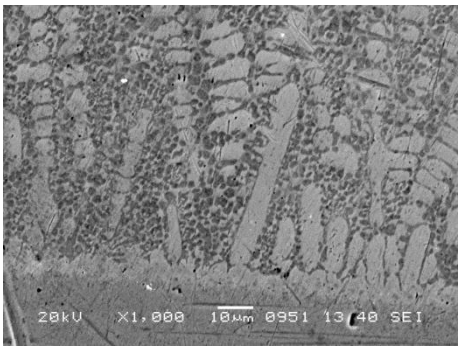

Figure 3. Typical microstructure at the junction between 316L SS substrate and cladding in sample LC1.

Figure 4 shows the typical OM diagram of the second cladding layer of LC1. It can be seen from the figure that there are two equiaxed crystal bands at the top and bottom, which are called bonding zones. As shown in Figure 4 (b) ~ (e), the enlarged structure of the lower bonding zone and the upper bonding zone respectively shows that the grains in the zone are obviously equiaxed (Figure 4 (b) and (E)), and the band between the second and third layers has a wider scale. In the middle of the second cladding layer, columnar dendrites and some equiaxed dendrites are obvious (Figure 4 (c) and (d)).

The formation of the bonding zone is the result of reheating at the top of the first and second layers. During multiple cladding, the top of the upper layer is melted, and the area below the top is reheated, resulting in grain growth in this area [31]. When it comes to columnar dendrites and equiaxed dendrites, they can still be described by the change of temperature G/R ratio. After cellular crystals appear, columnar dendrites are formed with the further decrease of G/R ratio. At low G/R ratio, columnar dendrites transform into equiaxed dendrites (CET) and equiaxed dendrites are formed [30, 31]. There is no planar crystal and cellular crystal at the bottom of the second cladding layer, which is due to the rapid solidification rate, which does not have enough time to stably grow into plane crystal and cellular crystal [32]. Of course, the heat accumulation during the second layer cladding is also a factor that has to be considered. Due to the heat accumulation, the temperature gradient at the bottom of the molten pool decreases, resulting in the decrease of G/R ratio, which is easier to form columnar dendrites. The closer to the middle of the bath, the smaller the G/R ratio is, and finally equiaxed dendrites are formed due to CET. In addition, some oblique growing dendrites were observed below the bonding zone, which generally appeared near the top of the molten pool, which was caused by the movement of laser beam and the contact with air, resulting in the change of the direction of temperature gradient; at the same time, the flow in the molten pool also caused the dendrite to deflect during the growth process.

Preprints (www.preprints.org) | NOT PEER-REVIEWED | Posted: 22 December 2020 doi:10.20944/preprints202012.0549.v1

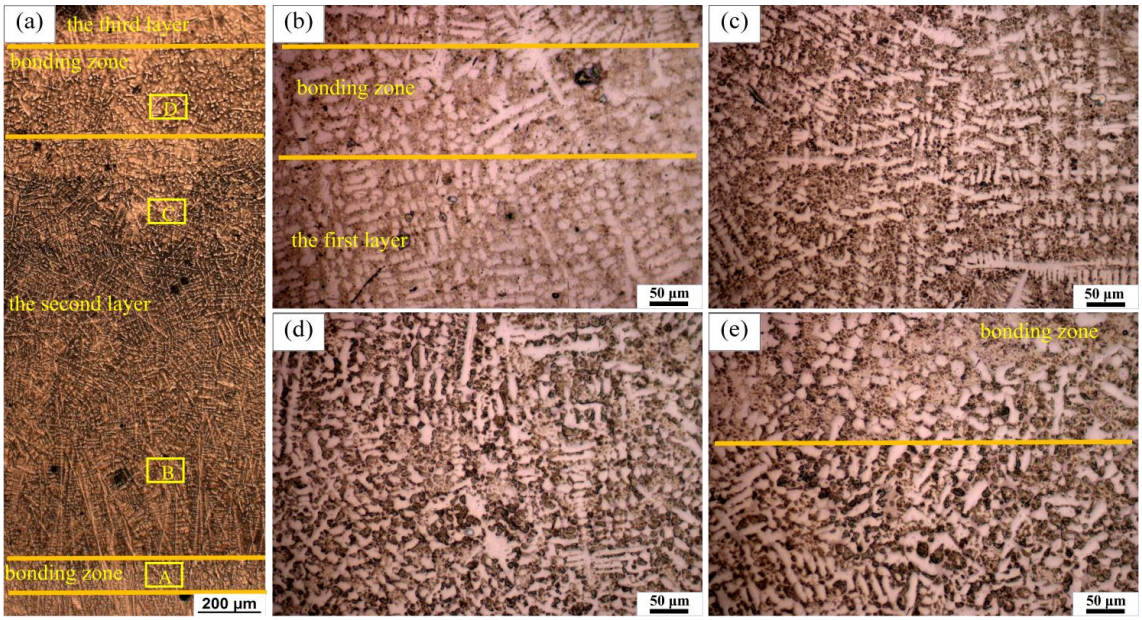

Figure 4. Typical microstructure of the second cladding in sample LC1: (b)~(e) correspond to A ~ D in (a) respectively.

The microstructure and morphology of the interface of the second and third layers of the three samples are basically similar to the above analysis, but there are still some differences (Figure 5). In LC2 and LC3, there are a large area of equiaxed grains under the bonding zone. With the increase of laser power and cladding layer, the heat accumulation increases, the G/R ratio decreases, and more equiaxed grains are formed. On the other hand, the smaller G/R ratio caused by more geothermal accumulation will also enable more columnar dendrites to be observed. However, the more complex temperature gradient will make the directional distribution of columnar crystal more complex.

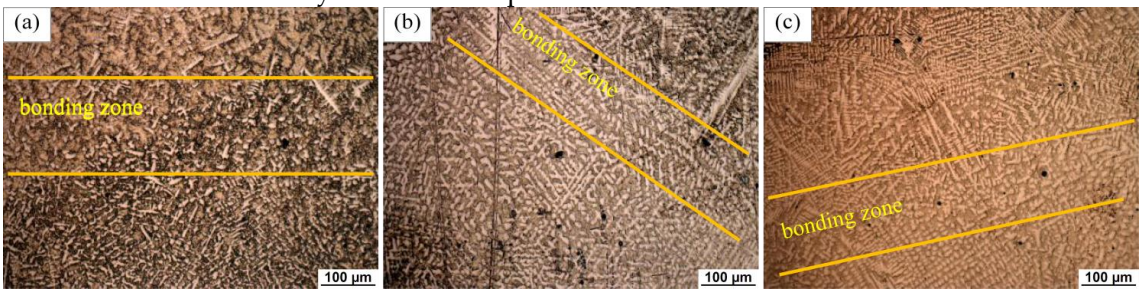

Figure 5. Microstructure of the bonding zone between the second and third layers in (a) sample LC1; (b) LC2; (c) LC3.

3.2 Phase composition and analysis

XRD diffraction was used to analyze the phase composition of Ni based alloy powder and cladding layer, and the results are shown in Figure 6. It can be seen from the figure that the main phases in the alloy powder are γ - Ni, Ni_3B, Cr_5B_3 and $Ni_{17}Si_3$. After laser cladding, it is obvious that many small peaks disappear, but there is no significant difference in the phase of the three cladding layers under different power. However, there is a main peak at 51-52 ° in sample LC1, and the peak at the corresponding position is a secondary strong peak in both powder and LC2 and LC3, which may be due to the preferred orientation in the sample structure under the cladding condition. For face centered cubic structure, the preferred growth direction is < 100 > orientation group. However, in different laser cladding processes, the complex temperature gradient, heat dissipation direction and solidification speed will affect the crystal growth. Finally, the crystal will choose the direction with the smallest angle between the

Preprints (www.preprints.org) | NOT PEER-REVIEWED | Posted: 22 December 2020 doi:10.20944/preprints202012.0549.v1

solid-liquid interface front velocity and the front velocity. In addition, the γ - Ni peak shifts to the left in the cladding layer, which is attributed to the lattice distortion caused by the solid solution of more alloy elements into the γ-Ni solid solution during rapid melting and cooling [33]. It can be seen that the main phases in the cladding layer are γ - Ni solid solution, Ni_3B, Cr_5B_3 and $Ni_{17}Si_3$. Among them, borides such as Ni_3B and Cr_5B_3 can provide good hardness and wear resistance for the cladding layer. Other elements, such as Fe and C, have not been determined due to their low contents.

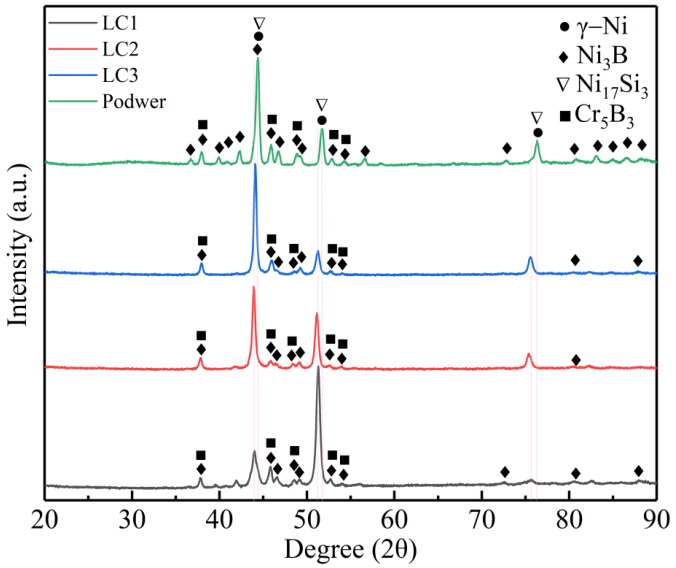

Figure 6. XRD patterns of powders and three cladding coatings.

The microstructure of the cladding layer was observed and analyzed by SEM, as shown in Figure 7, the SEM pictures of the middle part of the second layer cladding layer of three kinds of samples were shown. It can be seen that sample LC2 has more coarse dendrite than sample LC1 and sample LC3, which is due to the increase of input power, the corresponding heat input will also increase, and the solidification rate will decrease, which is conducive to the growth of dendrite. However, with the further increase of the input power, the heat input continues to increase, and the heat accumulation increases. When the G/R ratio is small, it is easier to form equiaxed dendrites, and the dense equiaxed dendrites restrict each other during the growth process, which makes the grains smaller.

In addition, the microstructure near the surface of the third cladding layer was observed, as shown in Figure 8. In the structure near the outer surface of LC1, no obvious dendrite morphology was observed, but strip-shaped phase and honeycomb structure could be seen. The elements in the strip phase were analyzed by EDS in Figure 9. the results show that the strip phase is rich in Ni, Si and Fe elements. However, the dendrite morphology can still be observed in LC2 and LC3, and the network structure can also be observed in the interdendritic zone. Such network structure can also be observed in Figure 7 (a) and (b). EDS is used to analyze the elements of the network structure, and the results are shown in Figure 9. FE-SEM was used to observe the microstructure of Fig. 8 (a) ~ (c) in more detail. It can be seen from Figure 8 (d) ~ (f) that the honeycomb structure in sample LC1 is actually very fine. In the study of [34], there is also a small microstructure near the outer surface, which can provide higher hardness. The most obvious dendrite structure can be observed in LC3, and the network structure is distributed among the dendrites; compared with the finer microstructure, the coarse dendrite structure provides lower hardness.

Preprints (www.preprints.org) | NOT PEER-REVIEWED | Posted: 22 December 2020 doi:10.20944/preprints202012.0549.v1

According to the EDS results (Figure 9), the element C is mainly measured in the dendrites and also distributed in the interdendritic region, but it is difficult to detect in the interdendritic network structure. Si is mainly distributed in the network structure between dendrites, less in dendrites, and a little or no Si in interdendritic. There was no significant difference in the distribution of other elements. EDS showed similar distribution results in the three samples. However, only Ni, Fe and Si elements were detected in the long strip structure observed in LC1, and no other elements were detected. Combined with XRD results, it can be inferred that $Ni_{17}Si_3$ phase mainly exists in the interdendritic zone and network structure, especially in the network structure. As for the light element B, EDS has not been detected, but in the study of laser cladding Ni-Cr-B-Si-C on 316L SS by Jeyaprakash [4], it is reported that Ni3B and γ - Ni (Fe, Si, Cr) form interdendritic network eutectic structure.

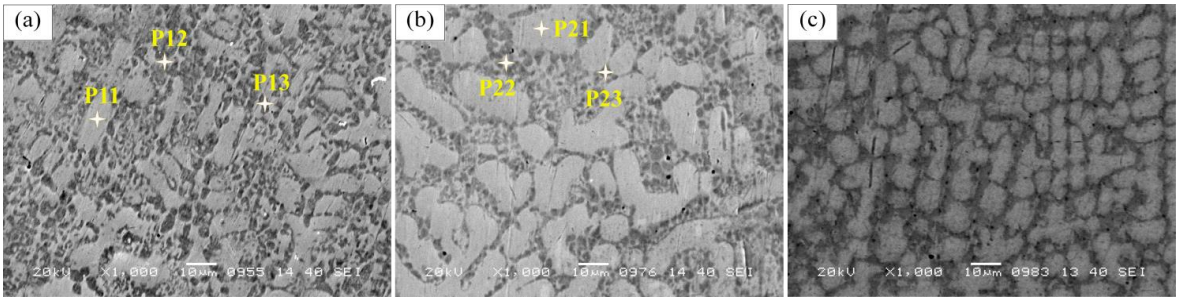

Figure7. SEM images of the middle region in the second cladding coating: (a) sample LC1; (b) LC2; (c) LC3.

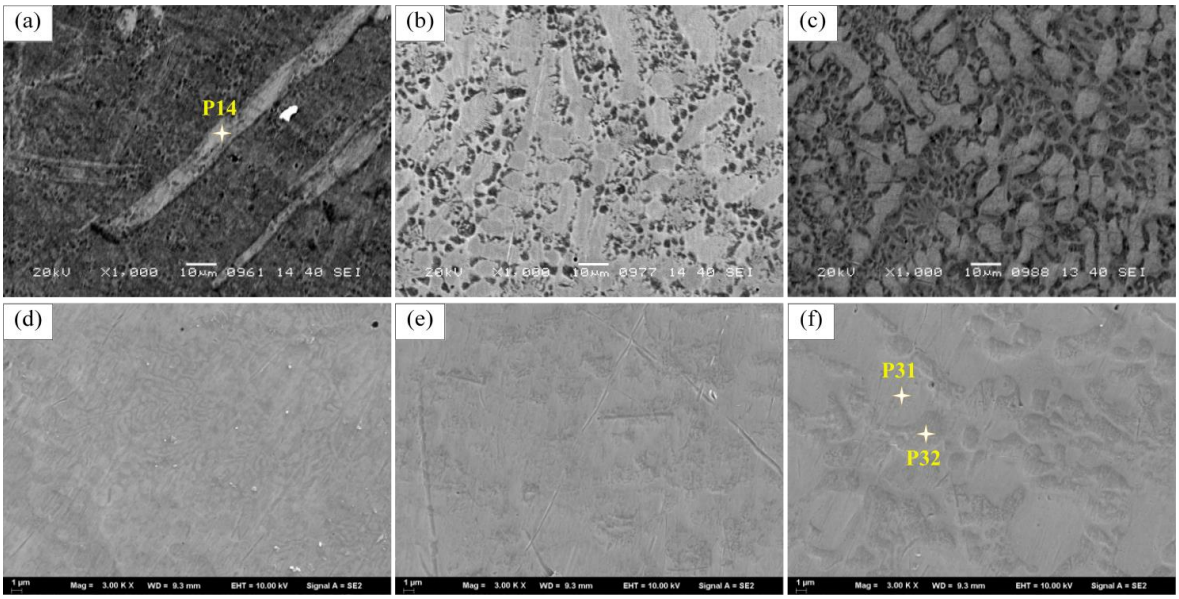

Figure 8. SEM and FE-SEM images of the surface region in the third cladding coatings: (a) sample LC1; (b) LC2; (c) LC3.

Preprints (www.preprints.org) | NOT PEER-REVIEWED | Posted: 22 December 2020 doi:10.20944/preprints202012.0549.v1

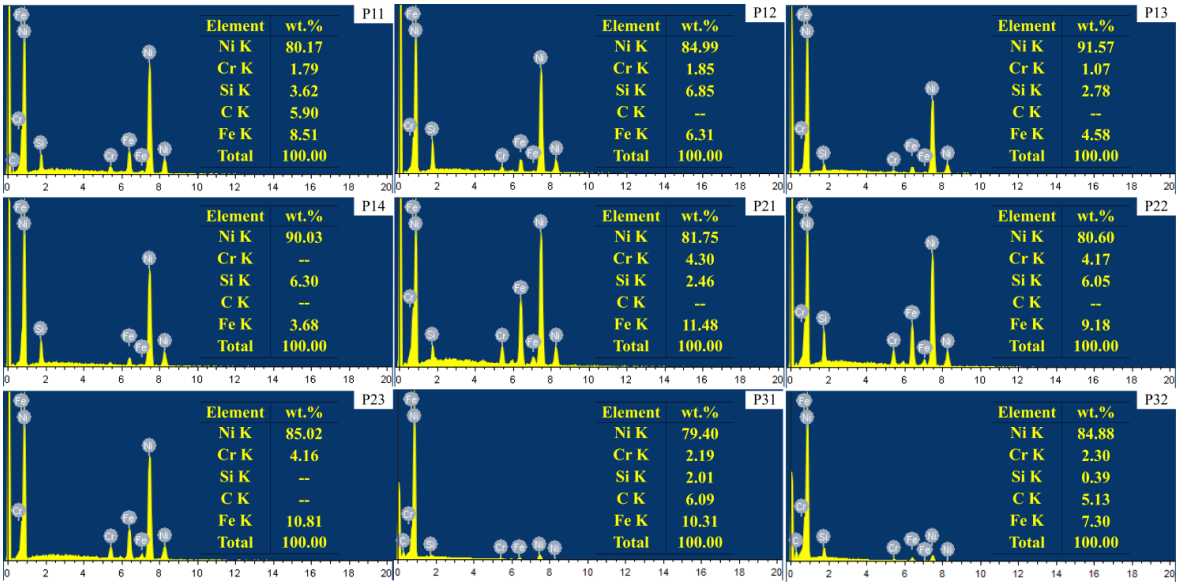

Figure 9. The Corresponding EDS results in Figure 8.

3.3 Microhardness and wear behavior

The microhardness of the cross section of the substrate and cladding layer was tested, as shown in Figure 10. As can be seen from it, the microhardness of 316L substrate is about 200 $HV_{0.2}$, and the hardness of cladding layer is significantly higher than that of substrate. At the same time, it can be seen from the figure that the microhardness of the substrate decreases slightly near the junction of the cladding layer and the substrate, which is due to the influence of temperature on the substrate during the cladding process. The microhardness of the cladding layer rises abruptly to about 600 $HV_{0.2}$ after crossing the interface. LC1 has the smallest microstructure near the outer surface, which contributes to the least fluctuation of hardness, followed by LC2 and LC3. According to the microhardness distribution curve of the cladding layer section, the microhardness of the inner region is slightly lower than that of the outer region, which is due to the coarser microstructure of the inner region. Figure 10 (b) shows the average hardness of the three cladding layers. It can be seen that the average hardness of the cladding layer can reach about 2.8 ~ 3.0 times of the substrate. In addition to the formation of residual stress during rapid cooling, the high hardness of cladding layer is attributed to the formation of γ-Ni solid solution formed by solid solution of alloy elements and the formation of intermetallic compounds $Ni_{17}Si_3$, Ni_3B and Cr_5B_3. With the increase of laser power, the average microhardness of cladding layer decreases, but the decreasing range gradually decreases. The maximum average hardness is LC1 (~ 605 HV0.2), which is due to the higher hardness contributed by finer microstructure. Then LC2 (~ 568 HV0.2) and minimum LC3 (~ 563 HV0.2).

Preprints (www.preprints.org) | NOT PEER-REVIEWED | Posted: 22 December 2020 doi:10.20944/preprints202012.0549.v1

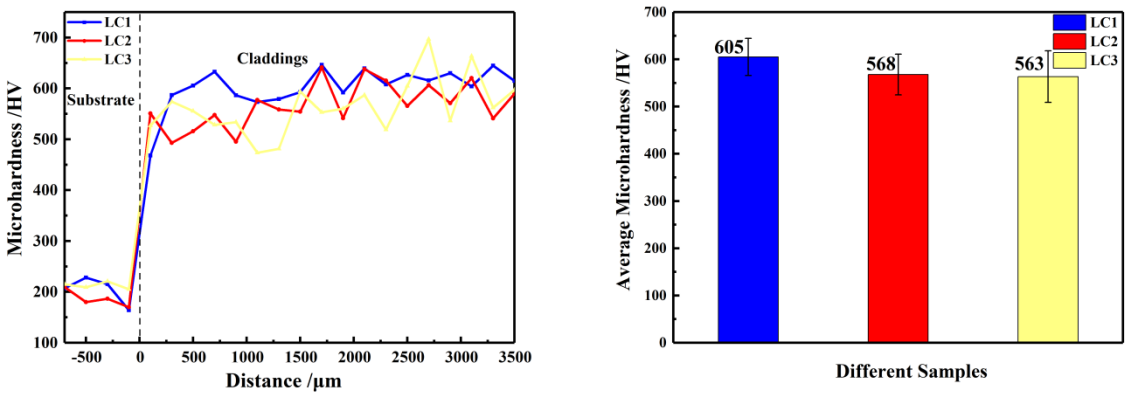

Figure 10. Vickers microhardness of the substrate and cladding coatings: (a) Microhardness distribution of cross section; (b) average microhardness.

Since the tribological properties are not the inherent properties of materials but depend on the mechanical properties, roughness, friction, and other factors [35, 36], the substrate and three cladding layers are polished under the same conditions, and the same experimental conditions are used to reduce the error of four samples in the friction test. Friction and wear experiments were carried out on the surface of substrate and multi-layer cladding layer. Figure 11 (a) and (b) show the friction coefficient curve and average friction coefficient of substrate and three kinds of cladding layer respectively. It can be seen from the curve that the friction coefficient of the substrate keeps a small fluctuation from the beginning to the end. This is due to the low C content in the microstructure of 316L stainless steel, which is mainly composed of austenite and a certain amount of ferrite, and there is no other hard and brittle phase in the soft structure, so the friction coefficient changes little during the friction process. In addition, the friction coefficient of the matrix has a tendency to decrease gradually (analyzed in the back wear scar morphology). However, the friction coefficients of the three cladding layers fluctuate greatly, which is due to the effect of debris falling off during the friction process; the fluctuation of LC1 is the most obvious (between 0.31 ~ 0.48), especially after the peak value, it drops sharply. The friction coefficient of LC2 and LC3 is more gentle than that of the cladding layer, and there is no abrupt drop after the peak value of LC1. The fluctuation range of LC2 wear coefficient is 0.28 ~ 0.42, and LC3 is 0.33 ~ 0.42. It can be seen from Figure 11 (b) that the average friction coefficients of matrix, LC1, LC2 and LC3 are 0.6316, 0.3702, 0.3544 and 0.3619, respectively, and the friction coefficient of matrix is about 1.7-1.8 times of that of three cladding layers.

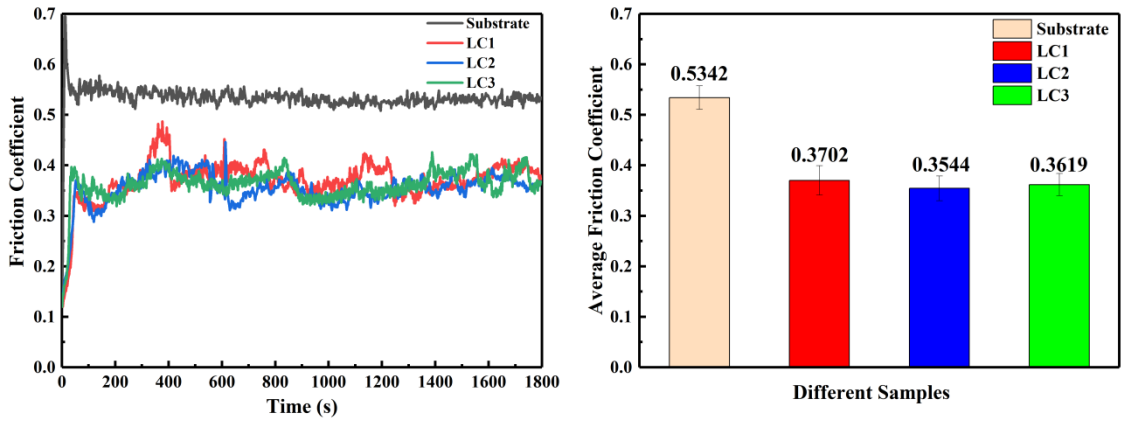

Preprints (www.preprints.org) | NOT PEER-REVIEWED | Posted: 22 December 2020 doi:10.20944/preprints202012.0549.v1

Figure 11. Friction coefficient of the substrate and cladding coatings: (a) friction coefficient curves; (b) average friction coefficient.

The three-dimensional morphology and the wear profile of the substrate and cladding layer are shown in Figure 12. It can be seen from the three-dimensional wear map of the substrate that there are a large number of protrusions and pits. The surface of the wear marks is uneven, and the material is extruded and piled up on both sides, showing ridge shape (Figure 12 (a)). In contrast, the scratch of cladding layer is smoother, and it is difficult to see uneven protrusion on the surface of wear mark of cladding layer, but there are some gullies and ridges. It can be seen from the contour curve of wear marks (Figure 12 (b)), that the wear scar width of substrate is ~ 2000 μm, which is much larger than ~ 450 μm of LC1, ~ 460 μm of LC2 and ~ 440 μm of LC3. The maximum wear scar depth of the substrate is ~ 38 μm, which is still far greater than ~ 7μ m of LC1, ~ 7μ m of LC2 and ~ 9μ m of LC3 (inset in Figure 12 (b)). After laser cladding, the surface of 316L stainless steel can be effectively protected.

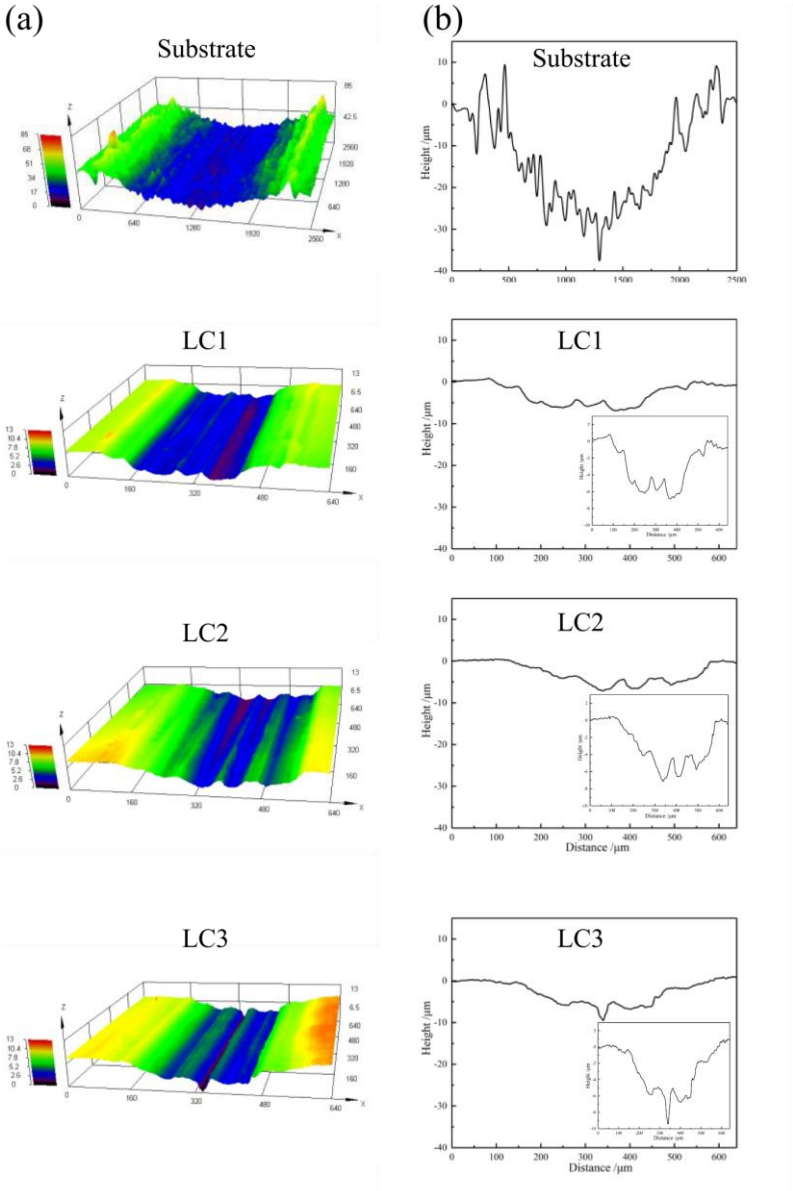

Figure 12. 3D morphology (a) and wear profiles (b) of the substrate and cladding coatings.

Figure 13 shows the SEM images of wear marks of substrate and cladding layer. As can be seen

 doi:10.20944/preprints202012.0549.v1

from Figure 13 (a), large grooves can be observed on the worn surface of the substrate. The appearance of such plough marks represents high plastic deformation and low wear resistance [37]. Due to the forced transfer of materials by ploughing, stacking / delamination of materials, as well as corresponding drop pits and spalling, can be observed. Small steps of transverse deformation layer formed by material transfer and flaking soft material influence friction process continuously. Relatively soft substrate, in the process of friction can produce new shedding materials, in the repeated wear of the friction ball back and forth, in addition to adhering to the wear surface, it can be used as abrasive to intensify the wear of substrate. With the increase of the number of cycles, the deformation layer can be transformed into a protective film to reduce the friction [38], which leads to the gradual decrease of friction coefficient. The corresponding phenomenon can be seen from the figure 11. However, this protection is negligible relative to wear, and the base material is still being worn. Generally speaking, the wear mechanism of the substrate is abrasive wear and adhesive wear.

Figure 13 (b) shows the wear morphology of LC1 cladding layer. It can be seen that there is also material stacking phenomenon in the wear morphology of the cladding layer, which is only longitudinal distribution, consistent with the wear direction, and there is no mass transfer of materials like the matrix. The appearance of the ridge is more caused by a small amount of material having to be extruded to both sides under the action of vertical stress and shear stress in the wear process, corresponding to the ridge dent morphology of the worn surface in the three-dimensional diagram (Figure 12). In addition, pits of different sizes due to peeling off, as well as small wear debris and mild groove, can be seen on the worn surface of LC1. This kind of not deep groove is mainly caused by the abrasive wear caused by small wear debris, which also represents that the cladding layer has good wear resistance. The same ridge morphology, fine wear debris and slight grooves can also be seen in the wear morphology of LC2 and LC3 cladding layers (Figure 13 (c) ~ (d)), indicating that the three coatings have similar good wear resistance. However, there are no large drop pits in LC2 and LC3 as shown in Figure 13 (b). Combined with the microstructure of LC1 cladding layer, it can be referred that there is a long strip phase in the outer surface structure of LC1. Due to the large aspect ratio, this long strip phase is easy to break and peel off from the cladding layer under the action of external stress. The material is dug out from the cladding layer by the falling debris in the process of continuous cyclic wear, resulting in large spalling pits. At the same time, this behavior will lead to the increase of friction coefficient, which will lead to the increase of friction coefficient. Of course, the average friction coefficient of LC1 is slightly higher than that of LC2 and LC3, although the friction coefficient generally decreases with the increase of hardness [39]. In a word, the main wear mechanism of cladding layer is abrasive wear. From the point of view of wear, the Ni based alloy coating can provide good protection for 316L stainless steel substrate, so as to avoid failure or damage due to a large number of wear in corresponding environment, and effectively improve the wear life of the material.

Preprints (www.preprints.org) | NOT PEER-REVIEWED | Posted: 22 December 2020 doi:10.20944/preprints202012.0549.v1

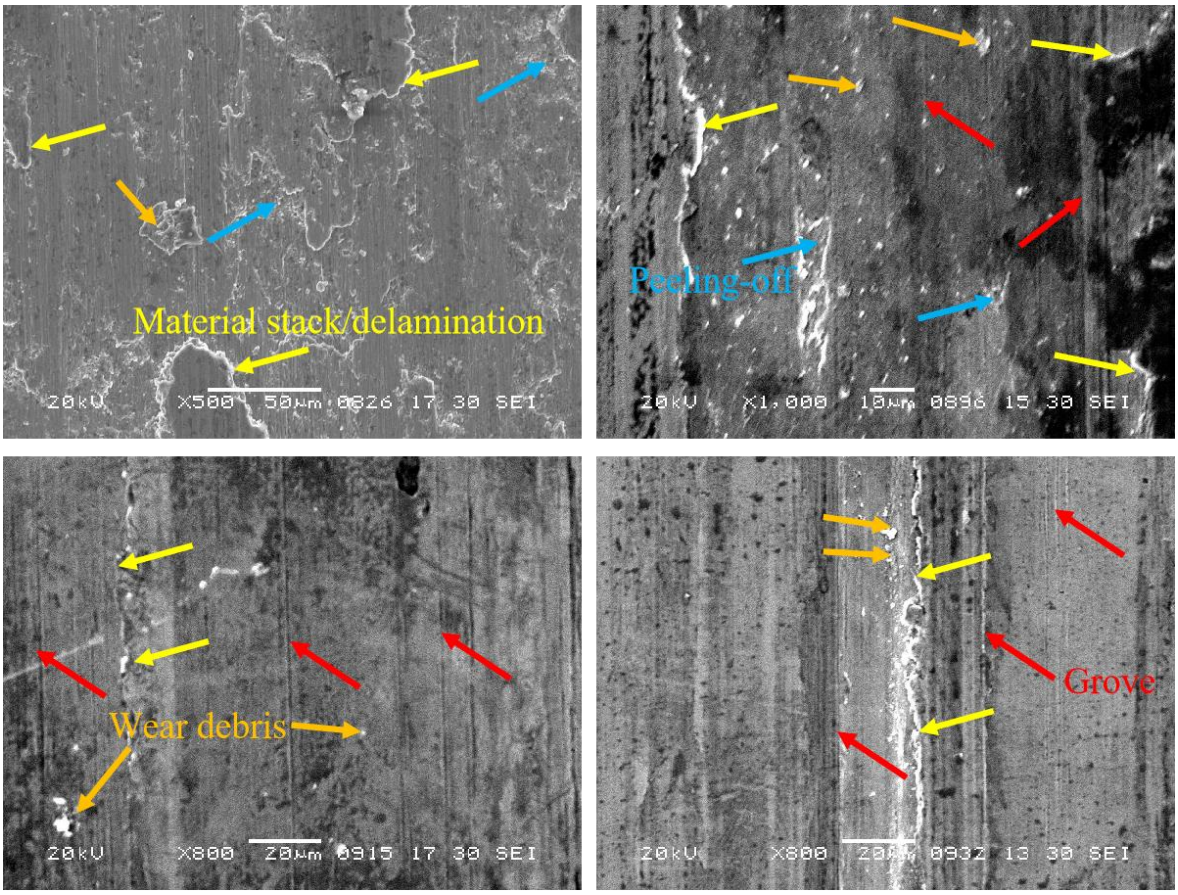

Figure 13. SEM images of worn surface morphology: (a) substrate; (b) sample LC1; (c) sample LC2; (d) sample LC3.

4. Conclusions

1. The bonding zone between cladding layers is observed, and the microstructure is coarse dendrite formed by reheating. The planar and cellular crystals observed at the substrate cladding interface were not observed in the subsequent cladding layer due to heat accumulation. More equiaxed dendrites can be observed in the cladding layer, and more coarse columnar dendrites can be observed in the bonding zone.

2. There is no significant difference in the composition of the three kinds of cladding layers, and the main phases are γ-Ni, Ni_3B, Cr_5B_3 and $Ni_{17}Si_3$. EDS results show that C element mainly exists in the dendrite, while Si element mainly distributes in the network structure and dendrite between the dendrites, and there is no obvious difference in the distribution of other elements. In addition, only Ni, Si and Fe were detected in the long strip phase near the outer surface of LC1.

3. The average hardness of the cladding layer is about 2.8 ~ 3.0 times of that of the substrate, which can be attributed to the formation of γ-Ni solid solution and intermetallic compounds $Ni_{17}Si_3$, Ni_3B and Cr_5B_3. The microhardness of the inner region is slightly lower than that of the outer region, and the hardness of LC1 is higher than that of LC2 and LC3, which can be explained according to the microstructure.

4. The friction coefficient of the substrate is about 1.7 ~ 1.8 times of that of the cladding layer. The wear mechanism of the substrate is mainly abrasive wear and adhesive wear, while the main wear mechanism of the cladding layer is abrasive wear. The cladding layer can provide good protection.

Reference

1. Wang, Q.-Y.; Wang, X.-Z.; Luo, H.; Luo, J.-L., A study on corrosion behaviors of Ni–Cr–Mo laser coating, 316 stainless steel and X70 steel in simulated solutions with H_2S and CO_2. *Surface and Coatings Technology* **2016,** 291, 250-257.
2. Ertugrul, O.; Enrici, T. M.; Paydas, H.; Saggionetto, E.; Boschini, F.; Mertens, A., Laser cladding of TiC reinforced 316L stainless steel composites: Feedstock powder preparation and microstructural evaluation. *Powder Technology* **2020,** 375, 384-396.
3. Maurizi Enrici, T.; Dedry, O.; Boschini, F.; Tchoufang Tchuindjang, J.; Mertens, A., Microstructural and Thermal Characterization of 316L+ WC Composite Coatings Obtained by Laser Cladding. *Advanced Engineering Materials* **2020**.
4. Jeyaprakash, N.; Yang, C.-H.; Sivasankaran, S., Laser cladding process of Cobalt and Nickel based hard-micron-layers on 316L-stainless-steel-substrate. *Materials and Manufacturing Processes* **2020,** 35, (2), 142-151.
5. Mészáros, L.; Kéldor, M.; Hidasi, B.; Vértes, A.; Czakó-Nagy, I., Micromagnetic and Mössbauer spectroscopic investigation of strain-induced martensite in austenitic stainless steel. *Journal of materials engineering and performance* **1996,** 5, (4), 538-542.
6. Liu, G.; Lu, J.; Lu, K., Surface nanocrystallization of 316L stainless steel induced by ultrasonic shot peening. *Materials Science and Engineering: A* **2000,** 286, (1), 91-95.
7. Liu, Z.; Peng, Y.; Chen, C.; Gong, J.; Jiang, Y., Effect of surface nanocrystallization on low-temperature gas carburization for AISI 316L austenitic stainless steel. *International Journal of Pressure Vessels and Piping* **2020,** 182, 104053.
8. Lu, K.; Lu, J., Nanostructured surface layer on metallic materials induced by surface mechanical attrition treatment. *Materials Science and Engineering: A* **2004,** 375, 38-45.
9. Sun, Z.; Retraint, D.; Baudin, T.; Helbert, A.-L.; Brisset, F.; Chemkhi, M.; Zhou, J.; Kanouté, P., Experimental study of microstructure changes due to low cycle fatigue of a steel nanocrystallised by Surface Mechanical Attrition Treatment (SMAT). *Materials Characterization* **2017,** 124, 117-121.
10. Jiang, Y.; Li, Y.; Jia, Y.-F.; Zhang, X.-C.; Gong, J.-M., Gradient elastic–plastic properties of expanded austenite layer in 316L stainless steel. *Acta Metallurgica Sinica (English Letters)* **2018,** 31, (8), 831-841.
11. Jones, J. L.; Koul, M. G.; Schubbe, J. J., An evaluation of the corrosion and mechanical performance of interstitially surface-hardened stainless steel. *Journal of materials engineering and performance* **2014,** 23, (6), 2055-2066.
12. Maistro, G.; Perez-Garcia, S.; Norell, M.; Nyborg, L.; Cao, Y., Thermal decomposition of N-expanded austenite in 304L and 904L steels. *Surface engineering* **2017,** 33, (4), 319-326.
13. Morell-Pacheco, A.; Kim, H.; Wang, T.; Shiau, C.-H.; Balerio, R.; Gabriel, A.; Shao, L., Ni coating on 316L stainless steel using cage plasma treatment: Feasibility and swelling studies. *Journal of Nuclear Materials* **2020,** 540, 152385.
14. Bell, T., Surface engineering of austenitic stainless steel. *Surface Engineering* **2002,** 18, (6), 415-422.
15. Balla, V. K.; Das, M.; Bose, S.; Ram, G. J.; Manna, I., Laser surface modification of 316 L stainless steel with bioactive hydroxyapatite. *Materials Science and Engineering: C* **2013,** 33, (8), 4594-4598.
16. Yi, D., Development of a flame spraying coating–based fiber composite structure: A thermo-mechanical finite element study. *Journal of Intelligent Material Systems and Structures* **2020,** 31, (16), 1950-1958.

17. Smialek, J. L., Compiled furnace cyclic lives of EB-PVD thermal barrier coatings. *Surface and Coatings Technology* **2015,** 276, 31-38.
18. Savanth, T.; Singh, J.; Gill, J., Laser power and scanning speed influence on the microstructure, hardness, and slurry erosion performance of Colmonoy-5 claddings. *Proceedings of the Institution of Mechanical Engineers, Part L: Journal of Materials: Design and Applications* **2020**, 1464420720922568.
19. Tromans, D., Elastic anisotropy of HCP metal crystals and polycrystals. *Int. J. Res. Rev. Appl. Sci* **2011,** 6, (4), 462-483.
20. Jeyaprakash, N.; Yang, C.-H.; Ramkumar, K., Microstructure and wear resistance of laser cladded Inconel 625 and Colmonoy 6 depositions on Inconel 625 substrate. *Applied Physics A* **2020,** 126, 1-11.
21. Yuan, W.; Li, R.; Chen, Z.; Gu, J.; Tian, Y., A comparative study on microstructure and properties of traditional laser cladding and high-speed laser cladding of Ni45 alloy coatings. *Surface and Coatings Technology* **2020**, 126582.
22. Alfred, I.; Nicolaus, M.; Hermsdorf, J.; Kaierle, S.; Möhwald, K.; Maier, H.-J.; Wesling, V., Advanced high pressure turbine blade repair technologies. *Procedia CIRP* **2018,** 74, 214-217.
23. Mertens, A.; L'Hoest, T.; Magnien, J.; Carrus, R.; Lecomte-Beckers, J. In *On the elaboration of metal-ceramic composite coatings by laser cladding*, Materials Science Forum, 2017; Trans Tech Publ: pp 1288-1293.
24. Zhai, Y.-J.; Liu, X.-B.; Qiao, S.-J.; Wang, M.-D.; Lu, X.-L.; Wang, Y.-G.; Chen, Y.; Ying, L.-X., Characteristics of laser clad α-Ti/TiC+ (Ti, W) C1− x/Ti2SC+ TiS composite coatings on TA2 titanium alloy. *Optics & Laser Technology* **2017,** 89, 97-107.
25. Feng, K.; Chen, Y.; Deng, P.; Li, Y.; Zhao, H.; Lu, F.; Li, R.; Huang, J.; Li, Z., Improved high-temperature hardness and wear resistance of Inconel 625 coatings fabricated by laser cladding. *Journal of Materials Processing Technology* **2017,** 243, 82-91.
26. Janicki, D., Laser cladding of Inconel 625-based composite coatings reinforced by porous chromium carbide particles. *Optics & Laser Technology* **2017,** 94, 6-14.
27. Chang, Z.; Wang, W.; Ge, Y.; Zhou, J.; Cui, Z., Microstructure and mechanical properties of Ni-Cr-Si-B-Fe composite coating fabricated through laser additive manufacturing. *Journal of Alloys and Compounds* **2018,** 747, 401-407.
28. Moskal, G.; Niemiec, D.; Chmiela, B.; Kałamarz, P.; Durejko, T.; Ziętala, M.; Czujko, T., Microstructural characterization of laser-cladded NiCrAlY coatings on Inconel 625 Ni-based superalloy and 316L stainless steel. *Surface and Coatings Technology* **2020,** 387, 125317.
29. Li, K.; Li, D.; Liu, D.; Pei, G.; Sun, L., Microstructure evolution and mechanical properties of multiple-layer laser cladding coating of 308L stainless steel. *Applied surface science* **2015,** 340, 143-150.
30. Kou, S., Welding metallurgy. *New Jersey, USA* **2003**, 431-446.
31. Luo, K.; Xu, X.; Zhao, Z.; Zhao, S.; Cheng, Z.; Lu, J., Microstructural evolution and characteristics of bonding zone in multilayer laser cladding of Fe-based coating. *Journal of Materials Processing Technology* **2019,** 263, 50-58.
32. Lin, X.; Yang, H.; Chen, J.; Huang, W., Microstructure evolution of 316L stainless steel during laser rapid forming. *ACTA METALLURGICA SINICA-CHINESE EDITION-* **2006,** 42, (4), 361.
33. Cui, G.; Han, B.; Zhao, J.; Li, M., Comparative study on tribological properties of the sulfurizing layers on Fe, Ni and Co based laser cladding coatings. *Tribology International* **2019,** 134, 36-49.
34. Saeedi, R.; Razavi, R. S.; Bakhshi, S. R.; Erfanmanesh, M.; Bani, A. A., Optimization and characterization of laser cladding of NiCr and NiCr–TiC composite coatings on AISI 420 stainless steel. *Ceramics International* **2020**.

 doi:10.20944/preprints202012.0549.v1

35. Hu, Z.; Li, W.; Zhao, Y., The Effect of Laser Power on the Properties of M3B2-Type Boride-Based Cermet Coatings Prepared by Laser Cladding Synthesis. *Materials* **2020,** 13, (8), 1867.
36. Ju, H.; Ding, N.; Xu, J.; Yu, L.; Geng, Y.; Ahmed, F.; Zuo, B.; Shao, L., The influence of crystal structure and the enhancement of mechanical and frictional properties of titanium nitride film by addition of ruthenium. *Applied Surface Science* **2019,** 489, 247-254.
37. Jeyaprakash, N.; Yang, C.-H.; Duraiselvam, M.; Prabu, G., Microstructure and tribological evolution during laser alloying WC-12% Co and Cr3C2− 25% NiCr powders on nodular iron surface. *Results in Physics* **2019,** 12, 1610-1620.
38. Upadhyay, R. K.; Kumar, A., Scratch and wear resistance of additive manufactured 316L stainless steel sample fabricated by laser powder bed fusion technique. *Wear* **2020,** 458, 203437.
39. Xiang, L.; Shen, Q.; Zhang, Y.; Bai, W.; Nie, C., One-step electrodeposited Ni-graphene composite coating with excellent tribological properties. *Surface and Coatings Technology* **2019,** 373, 38-46.